SUBMITTED TO APJ
Preprint typeset using LaTeX style emulateapj v. 5/2/11

DIRECT MEASUREMENT OF DUST ATTENUATION IN $z \sim 1.5$ STAR-FORMING GALAXIES FROM 3D-HST: IMPLICATIONS FOR DUST GEOMETRY AND STAR FORMATION RATES

SEDONA H. PRICE[1,*], MARISKA KRIEK[1], GABRIEL B. BRAMMER[2], CHARLIE CONROY[3], NATASCHA M. FÖRSTER SCHREIBER[4], MARIJN FRANX[5], MATTIA FUMAGALLI[5], BRITT LUNDGREN[6], IVELINA MOMCHEVA[7], ERICA J. NELSON[7], HANS-WALTER RIX[8], ROSALIND E. SKELTON[9], PIETER G. VAN DOKKUM[7], KATHERINE E. WHITAKER[10], STIJN WUYTS[4]

Submitted to ApJ

ABSTRACT

The nature of dust in distant galaxies is not well understood, and until recently few direct dust measurements have been possible. We investigate dust in distant star-forming galaxies using near-infrared grism spectra of the 3D-HST survey combined with archival multi-wavelength photometry. These data allow us to make a direct comparison between dust towards star-forming regions (measured using Balmer decrements) and the integrated dust properties (derived by comparing spectral energy distributions [SEDs] with stellar population and dust models) for a statistically significant sample of distant galaxies. We select a sample of 163 galaxies between $1.36 \leq z \leq 1.5$ with Hα SNR ≥ 5 and measure Balmer decrements from stacked spectra. First, we stack spectra in bins of integrated stellar dust attenuation, and find that there is extra dust extinction towards star-forming regions ($A_{\rm V,HII}$ is 1.81 times the integrated $A_{\rm V,star}$), though slightly lower than found for low-redshift starburst galaxies. Next, we stack spectra in bins of specific star formation rate (log sSFR), star formation rate (log SFR), and stellar mass ($\log M_*$). We find that on average $A_{\rm V,HII}$ increases with SFR and mass, but decreases with increasing sSFR. The amount of extra extinction also decreases with increasing sSFR and decreasing stellar mass. Our results are consistent with the two-phase dust model – in which galaxies contain both a diffuse and a stellar birth cloud dust component – as the extra extinction will increase once older stars outside the star-forming regions become more dominant. Finally, using our Balmer decrements we derive dust-corrected Hα SFRs, and find evidence that SED fitting produces incorrect SFRs if very rapidly declining SFHs are included in the explored parameter space.

Subject headings: dust, extinction — galaxies: evolution — galaxies: high-redshift

1. INTRODUCTION

While dust makes up only a very small fraction of the baryonic mass in galaxies (Draine et al. 2007), it can leave a large signature on the spectral energy distributions (SEDs). Dust extinguishes light in a wavelength-dependent way, which distorts the intrinsic SED of most galaxies. The dust extinction as a function of wavelength must be well understood before the intrinsic SED can be recovered from observations. The total dust attenuation in a galaxy also depends on the dust geometry. Developing a complete model of dust properties and distribution in galaxies thus requires observations of both the integrated dust properties and the dust towards star-forming regions.

* sedona@berkeley.edu
[1] Astronomy Department, University of California, Berkeley, CA 94720, USA
[2] Space Telescope Science Institute, 3700 San Martin Drive, Baltimore, MD 21218, USA
[3] Department of Astronomy & Astrophysics, University of California, Santa Cruz, CA 95064, USA
[4] Max-Planck-Institut für extraterrestrische Physik, Giessenbachstrasse, D-85748 Garching, Germany
[5] Leiden Observatory, Leiden University, P.O. Box 9513, 2300 RA Leiden, The Netherlands
[6] Department of Astronomy, University of Wisconsin, 475 N Charter Street, Madison, WI 53706, USA
[7] Department of Astronomy, Yale University, New Haven, CT 06511, USA
[8] Max-Planck-Institut für Astronomy, Königstuhl 17, D-69117 Heidelberg, Germany
[9] South African Astronomical Observatory, P.O. Box 9, Observatory 7935, South Africa
[10] Astrophysics Science Division, Goddard Space Flight Center, Code 665, Greenbelt, MD 20771, USA

The properties of dust in low-redshift galaxies have been extensively studied. The integrated dust attenuation ($A_{\rm V,star}$, which affects the continuum light in a galaxy) has been measured with three general methods: *(i)* the $L_{\rm IR}/L_{\rm UV}$ ratio (also known as IRX), which probes dust attenuation using energy conservation. This ratio is directly related to the UV continuum slope β (Meurer et al. 1999), which is used to infer the dust content for galaxies for which no IR data is available. The other methods are *(ii)* SED or color analysis using stellar population models, and *(iii)* line of sight analysis using a luminous background object (see Conroy 2013 for more discussion on this topic).

Dust extinction towards HII regions ($A_{\rm V,HII}$) is most directly probed with recombination line ratios, often using the Balmer decrement (Hα/Hβ). The intrinsic line ratio can be calculated given reasonable environmental parameters. As dust extinction is wavelength dependent, the measured line ratio compared with the intrinsic ratio combined with an assumed dust law yield a measure of the amount of dust attenuation towards star-forming regions. This method was used by Brinchmann et al. (2004) and Garn & Best (2010) to measure extinction towards star-forming regions for SDSS galaxies.

By comparing the two, Calzetti et al. (2000) find there is extra dust extinction towards star-forming regions relative to the integrated dust content for local starburst galaxies. Wild et al. (2011) expand on this by finding the amount of extra extinction increases with the axial ratio of galaxies, implying that the dust content of galaxies might have two phases (e.g. Calzetti et al. 1994; Charlot & Fall 2000; Granato et al. 2000): an optically thick component associated with the star-forming regions and a diffuse component distributed throughout the

ISM.

At higher redshifts, the nature of dust is much more poorly understood. Most work on dust in high-z galaxies has focused on the UV slope (e.g. Reddy et al. 2006; Reddy et al. 2010; Wilkins et al. 2011; Bouwens et al. 2012; Finkelstein et al. 2012; Reddy et al. 2012; Hathi et al. 2013, also see Shapley 2011 for a comprehensive review), as this is relatively easy to observe. However, deviations from the Meurer et al. (1999) IRX-β relation have been found for galaxy samples with different properties (e.g. Kong et al. 2004; Johnson et al. 2007; Conroy et al. 2010; Gonzalez-Perez et al. 2013), so using the UV slope to measure the continuum dust attenuation likely requires careful calibration. Indirect methods for measuring the attenuation towards HII regions have also been explored, relying on metallicity (e.g. Sobral et al. 2012), IR luminosity (e.g. Ibar et al. 2013), and comparison of SFR indicators (e.g. Wuyts et al. 2013).

Direct dust measurements toward HII regions using Balmer decrements are very challenging for $z > 0.5$ as both Hα and Hβ are shifted to the less-accesible near-infrared window. Careful survey design and instrument improvements have made measurements of the Balmer decrement possible for larger samples of intermediate redshift galaxies, e.g. between $0.4 \lesssim z \lesssim 1$ (Savaglio et al. 2005), $z \sim 0.5$ (Ly et al. 2012), and $z \sim 0.8$ (Villar et al. 2008; Momcheva et al. 2013). However, until recently Balmer decrements have been measured for only a small number of more distant galaxies (e.g. Teplitz et al. 2000; van Dokkum et al. 2005; Hainline et al. 2009; Yoshikawa et al. 2010).

Interestingly, current studies of dust properties in distant star-forming galaxies yield contrasting results. There is evidence for no extra extinction towards star-forming regions from Erb et al. (2006b) and Reddy et al. (2010), as extra extinction leads to an overestimate of the Hα SFR relative to the UV slope SFR. However, other studies find evidence that there is extra extinction. Förster Schreiber et al. (2009) compare measured and predicted $L_{\rm H\alpha}$ and Hα equivalent widths and find the best agreement when $A_{\rm V,HII}$ includes extra extinction relative to $A_{\rm V,star}$. A comparison of overlapping objects with Erb et al. (2006b) finds that the previous aperture corrections might be overestimated, which could mask some extra extinction. Yoshikawa et al. (2010) compare $A_{\rm V,star}$ from SED fitting and $A_{\rm V,HII}$ from Balmer decrements for a small sample and find the high-z objects are consistent with the local universe Calzetti et al. (2000) prescription for extra dust attenuation. Additionally, Wuyts et al. (2011b; 2013) find the best agreement between Hα SFRs and UV+IR SFRs when extra extinction is adopted, either the same as the local relation (Wuyts et al. 2011b) or a slightly lower ratio (Wuyts et al. 2013). Mancini et al. (2011) also compare SFRs and find the best agreement between Hα SFRs and SED SFRs is obtained when the local universe prescription for extra dust extinction is adopted. Recently, Kashino et al. (2013) use SFR comparisons and the Balmer decrement for a relatively large (although targeted) sample and find the amount of extra extinction is lower than the local relation.

These contrasting results may not be surprising, given the different and indirect methods and/or small and biased samples of most studies. Direct measurements of a statistical sample of distant galaxies are required to clarify these dust properties. This is now possible, as new IR instruments with multiple object spectroscopy capabilities are able to measure the Balmer decrement for even larger and more complete samples of high-redshift objects. In particular, the *Hubble Space Telescope*'s WFC3/G141 grism filter provides slitless spectra, allowing for a non-targeted survey of a large number of high-redshift galaxies. The *HST* grisms also avoid atmospheric near-IR absorption.

A number of surveys, including the 3D-HST survey (van Dokkum et al. 2011; Brammer et al. 2012), CANDELS (Koekemoer et al. 2011), and the WISP survey (Atek et al. 2010), have taken advantage of the *HST* grism capabilities to survey high redshift galaxies. Domínguez et al. (2013) were the first to use WFC3 grism data to make measurements of the Balmer decrement on a large, non-targeted sample. However, as their sample was not drawn from regions of the sky with existing deep photometric coverage, they were unable to examine trends of dust versus integrated galaxy properties.

We present a statistical study of dust extinction measured using the Balmer decrement for a large, non-targeted sample of galaxies at $z \sim 1.5$. Both rest-frame optical spectra and deep photometry are available, allowing us to compare extinction towards HII regions with a number of integrated galaxy properties.

Throughout this paper we adopt a ΛCDM universe with $\Omega_m = 0.3$, $\Omega_\Lambda = 0.7$, and $H_0 = 70\,{\rm km\,s^{-1}\,Mpc^{-1}}$.

2. DATA

2.1. *Observations and catalog*

Our sample is drawn from the 3D-HST survey (Brammer et al. 2012), a *Hubble Space Telescope (HST)* Treasury program adding ACS and WFC3 grism observations to the well-covered CANDELS (Koekemoer et al. 2011) fields: AEGIS, COSMOS, GOODS-S, and UDS. The 3D-HST data also include observations of the GOODS-N field from program GO-11600 (PI: B. Weiner).

The 3D-HST survey provides spatially resolved slitless grism spectra with ACS/G800L and WFC3/G141. In this work we only use the WFC3/G141 grism spectra, which covers $1.1\mu{\rm m} < \lambda < 1.65\mu{\rm m}$. The raw grism dispersion is $46.5\,{\rm pixel^{-1}}$, but interlacing during data reduction improves the dispersion to $\sim 23\,{\rm pixel^{-1}}$. The G141 grism has a maximum resolution of $R \sim 130$, corresponding to ~ 110 in the middle of our wavelength range.

The 3D-HST survey makes use of existing deep photometric coverage in each of the survey fields, combining the grism spectra with the publicly available, multi-wavelength photometric catalogs of AEGIS and COSMOS (Whitaker et al. 2011), GOODS-N (Kajisawa et al. 2011), GOODS-S (Wuyts et al. 2008), and UDS (Williams et al. 2009).

A modified version of the EAZY code (Brammer et al. 2008) is used on the combined grism spectra + photometry to measure the redshifts, emission line fluxes, and rest-frame U, V, J fluxes of the 3D-HST galaxies. Stellar masses, integrated dust extinction, SFRs, and sSFRs are determined by fitting stellar population synthesis models to the photometric data using the FAST code (Kriek et al. 2009). We use a separate set of parameters than those used by Brammer et al. (2012), for reasons discussed in Section 4.4. We use the Bruzual & Charlot (2003) stellar population synthesis models, assuming a Chabrier (2003) stellar initial mass function, solar metallicity, an exponentially declining star formation history with a minimum e-folding time of $\log_{10}(\tau_{\rm min}/{\rm yr}) = 8.5$, a minimum age of 40 Myr, and an integrated dust extinction $A_{\rm V}$ between 0 and 4 assuming the dust attenuation law by Calzetti et al. (2000).

Brammer et al. (2012) provide complete details on the 3D-

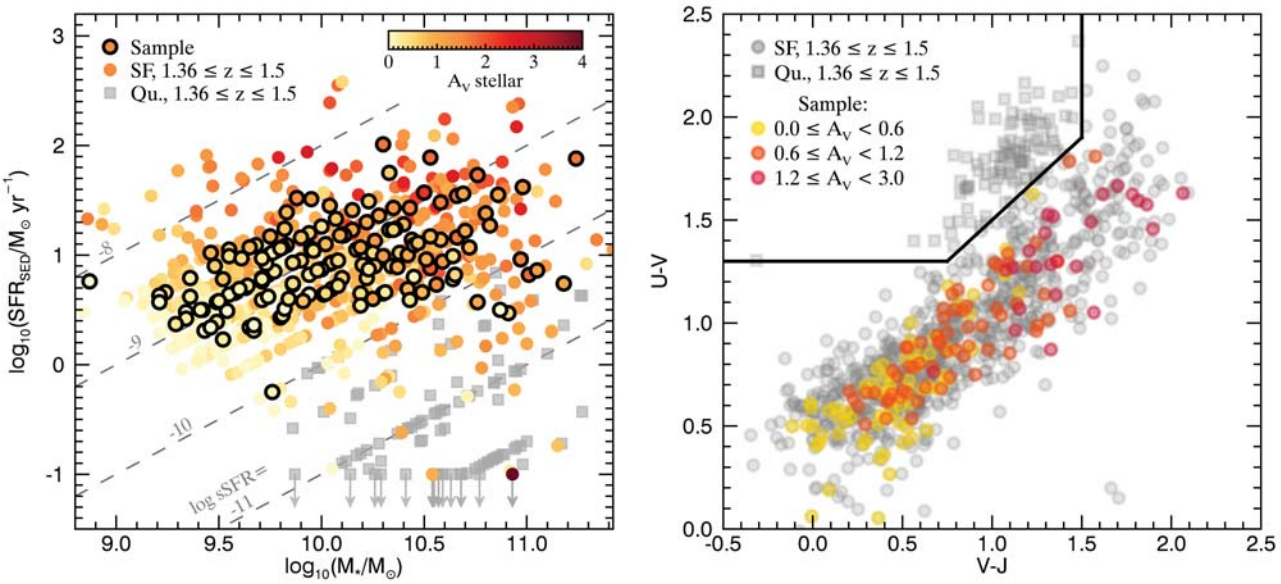

FIG. 1.— Sample characteristics relative to all 3D-HST galaxies in the same redshift range. The left panel shows $\log M_*$ vs. log SFR (from SED fitting) for all 3D-HST galaxies at $1.36 \leq z \leq 1.5$. The black circles indicate the sample selected for direct Balmer decrement measurements, consisting of galaxies with a strong Hα detection (i.e. S/N ≥ 5). Colors indicate the stellar A_V of the best-fit SED models found using the grism spectra and the photometry, as described in Section 2.1. The grey dashed lines show constant values of log sSFR. The right panel presents the rest-frame U-V and V-J colors for all 3D-HST galaxies between $1.36 \leq z \leq 1.5$ (in grey) and our sample (color-coded by stellar A_V bin). We discard any galaxies lying within the quiescent box (using the definition from Whitaker et al. 2012a) from our sample, as the emission lines for these galaxies likely originate from AGNs. In both panels, objects within the quiescent box of the UVJ diagram are shown as grey squares, while star-forming objects are shown as circles.

HST survey data reduction and parameter measurement procedure.

2.2. *Sample selection*

We select galaxies in the redshift range $1.36 \leq z \leq 1.5$, for which Hα and Hβ are generously covered by the G141 grism. In addition we impose a SNR cut of Hα SNR ≥ 5, to measure a decent line signal. We make no Hβ SNR cut, to avoid biasing our sample against the dustiest galaxies.

We have a number of additional selection criteria, to ensure high quality of the spectra. First, to avoid line misidentification, the photometric and grism redshifts must have good agreement, i.e. $|z_{\rm phot} - z_{\rm grism}| \leq 0.2$. Second, the contamination from other sources may not exceed 15% (an issue because of the slitless nature of the grism spectra). Third, there must be grism coverage of at least 95% (which must include the Hα and Hβ lines). Fourth, no more than 50% of the spectrum may be flagged as problematic (due to bad pixels or cosmic rays) during reduction.

To study dust attenuation towards star forming regions, we do not want AGN to contaminate our emission lines. To reject AGN, we exclude any objects that have a detected X-ray luminosity $L_X > 10^{42}$ erg s^{-1} (Mendez et al. 2013; Rosario et al. 2013; Bauer et al. 2002) by matching against the Chandra Deep Field North and South surveys (Alexander et al. 2003; Xue et al. 2011) and the XMM-Newton serendipitous survey (Watson et al. 2009). Furthermore we reject all objects that fall within the Donley et al. (2012) IRAC AGN region, or that fall within the quiescent box in the UVJ diagram defined in Whitaker et al. (2012a) (as the line emission likely originates from an AGN).

Finally, we visually inspect the grism spectra and photometry of the preliminary sample to reject problematic objects (i.e. wrong line identification). Our final sample includes 163 galaxies. Figure 1 shows how our sample compares to the full galaxy distribution at a similar redshift. The selected galaxies all have relatively high SFRs, and lie along the "star-forming main sequence" (e.g., Noeske et al. 2007; Daddi et al. 2007; Wuyts et al. 2011a; Whitaker et al. 2012b; Nelson et al. 2013). The values for our sample fall in the range 0 to 2.3 for $A_{\rm V,\,star}$, -10.44 to -8.11 for log sSFR, -0.25 to 2.01 fo6r log SFR, and 8.87 to 11.24 for $\log_{10} M_*$.

2.3. *Stacking*

The spectra of individual galaxies in this sample are too noisy to get a clear measurement of the Balmer decrement, the ratio of the flux of Hα to Hβ ($F_{\rm H\alpha}/F_{\rm H\beta}$). Thus we bin galaxies by parameter (SED A_V, sSFR, SFR, stellar mass) and stack the spectra before measuring line fluxes.

We adopt a uniform methodology for stacking spectra within a bin. First, we only use the portion of the grism spectra that falls between 1.13μm and 1.65μm (observed wavelength) to avoid noise at the edge of the grism coverage. Then the individual spectra are continuum normalized by scaling the biweighted mean value of the flux between 5500 and 6000Å (rest-frame) to unity. The individual spectra are then interpolated onto a common rest-frame wavelength grid.

The normalized spectra are stacked and averaged based on the number of spectra contributing at each wavelength. The stacked flux errors are simulated using a Monte Carlo error estimation, assuming the errors are normally distributed on either side of the mean.

The best-fit stellar population models are sampled over the same wavelength regime as the original spectra and used as the continua. The continua are stacked in the same way: they are continuum normalized and interpolated onto a common rest-frame wavelength grid, then averaged together.

The spectra and photometry have a slightly different slope for most galaxies, which results in a tilt between the stacked spectra and the stacked continua. To correct for this tilt offset,

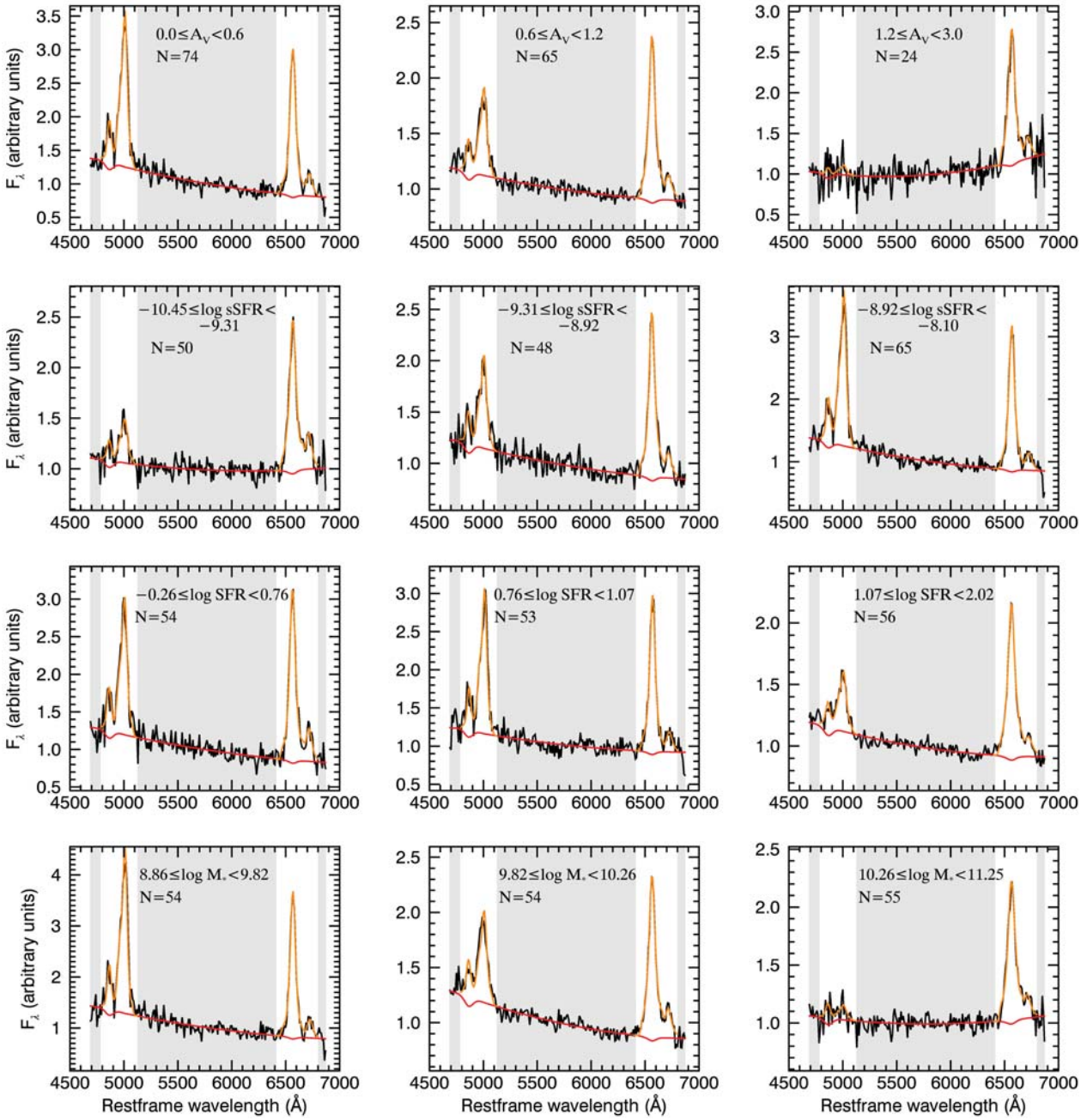

FIG. 2.— Stacked spectra for bins in stellar A_V (top), log sSFR (second row), log SFR (third row) and $\log M_*$ (bottom). In each panel, the stacked spectrum is plotted in black, with the continuum fit shown in red. The best fit line measurements (from shortest to longest wavelength: Hβ, [OIII]$\lambda\lambda$4959, 5007, blended Hα+[NII]$\lambda\lambda$6548, 6584, and [SII]$\lambda\lambda$6717, 6731) are shown in orange. The continuum fitting is done using the portions of the spectra within the shaded grey regions.

we fit a second-order Legendre polynomial to the continuum portions of the stacked spectrum (shown as the grey regions in Figure 2). We also fit the best-fit stellar population model, while masking the Balmer absorption features. The two polynomial fits are used to correct the tilt between the stacked continuum model and the stacked spectrum. The stacked, tilt-corrected continuum is subtracted from the stacked spectrum. This removes both the underlying continuum from our spectrum, and corrects for the intrinsic Balmer absorption of stellar atmospheres. The stacked spectra and tilt-corrected continua for the different bins are shown in Figure 2.

The adopted continuum normalization scheme leads objects with higher scaled Hα fluxes (the flux we measure after normalizing the spectrum) to have more weight in our line stack. To correctly compare the parameters from SED fitting ($A_{V,\,\rm star}$, stellar mass, SFR, sSFR) with values calculated from the stacked lines, we compute the weighted average of each parameter. We use the scaled Hα fluxes as the individual objects' weights. Errors on the average are estimated with bootstrapping.

2.4. *Line measurement*

To measure line fluxes, we fit each line in the continuum-subtracted stacked spectrum using least-squares minimiza-

tion. For our sample redshift range, the grism spectra have rest-frame coverage of the following spectral lines: Hβ, [OIII]$\lambda\lambda$4959, 5007, Hα, [NII]$\lambda\lambda$6548, 6584, and [SII]$\lambda\lambda$6717, 6731. However, the resolution of the grism data is insufficient for us to separate the Hα and [NII] lines, so we measure the blended Hα+[NII]$\lambda\lambda$6548, 6584 line.

The grism line shapes are not well described by gaussian profiles. Because the spatial resolution of the WFC3 detector ($\sim 0''.13\,\mathrm{pixel}^{-1}$) is much greater than the spectral resolution, the spectral line profiles are dominated by the object shapes. Thus, for each object we measure the object shape by summing the direct image (a postage stamp extracted from the F140W or F160W direct image) over the spatial direction (perpendicular to the dispersion direction) and use this as the line profile. The composite line profiles are created by flux-normalizing the individual profiles, multiplying each profile by the object's scaled Hα flux (described in Section 2.3), and finally averaging. This method yields a composite profile with the same effective weighting of the objects that results from the spectrum stacking method.

The grism spectra have roughly constant spectral resolution, so the composite line profiles described above have the correct width for an observed wavelength of 1.4 μm, or approximately Hα in the rest-frame for our redshift range. Thus for each line, we scale the line profile width by $\lambda_{\mathrm{line}}/\lambda_{\mathrm{H}\alpha}$.

Lines in a spectrum may not have the same profile, possibly due to dust or age gradients (e.g. Wuyts et al. 2012). However, the line fits obtained while using the same line profile (with appropriate width and amplitude scaling) match the data very well, suggesting that using a single profile for a stack is a reasonable approximation.

Because of the low spectral resolution of the grism spectra, we simultaneously fit the [OIII] doublet and Hβ, and similarly the blended Hα+[NII] line and the [SII] doublet. We fix the line ratio between [OIII]λ5007 and [OIII]λ4959 to 3:1 to reduce the number of degrees of freedom in our fit, and we fix the redshift of all lines to the value measured for Hα.

We compute the line fluxes from the best-fit line profile parameters. We then perform Monte Carlo simulations to estimate the flux errors. A simulated spectrum is generated using the continuum-subtracted stacked flux and errors. The continuum is remeasured and subtracted from the simulated spectrum, to include the error from the tilt-corrected continuum in the fits. The line fluxes are measured on the simulated spectrum following the same procedure detailed above. This process is repeated 500 times, and the upper and lower 1 σ errors are calculated from the set of fluxes measured from the simulations.

The best fit line measurements for our stacks are shown in Figure 2.

2.4.1. *[NII] correction*

To measure the Balmer decrement, we need to correct the blended Hα+[NII] line for the [NII] contribution. We use the stellar mass versus [NII]λ6584/Hα relation measured in Erb et al. (2006a) for galaxies at $z \sim 2$, as our sample covers a similar range of masses and SFRs, and are close in redshift.

The stellar masses Erb et al. (2006a) used are based on the integrated SFH, not the current stellar mass which we use. For the galaxies in our sample, which are all reasonably young, the mass from the integrated SFH is about 10% higher than the current stellar mass. We use this estimate to scale down the masses given by Erb et al. to match our stellar mass definition.

We interpolate the values Erb et al. report in Table 2 to estimate the ratio of [NII]λ6584/Hα with errors for the weighted average stellar mass in each bin. We assume an intrinsic line ratio of 3:1 between [NII]λ6584 and [NII]λ6548 to scale the ratio to include the second [NII] line. We use the interpolated and scaled ratio to calculate the Hα flux in each stack.

3. DUST EXTINCTION COMPARED WITH GALAXY PROPERTIES

3.1. *Measuring dust extinction towards star-forming regions*

The Balmer decrement, Hα/Hβ, lets us determine the amount of dust extinction towards star-forming regions by comparing the measured ratio with the expected line ratio given the physical conditions of the region. To calculate the dust extinction $A_{\mathrm{V,HII}}$ from the Balmer decrement, we follow the same method as used in Domínguez et al. (2013) and similar to the one used in Momcheva et al. (2013).

We assume that the HII region has a temperature $T = 10^4$ K, an electron density of $n_e = 10^2$ cm^{-3}, and the ions undergo case B recombination, so we assume an intrinsic ratio of $(\mathrm{H}\alpha/\mathrm{H}\beta)_{\mathrm{int}} = 2.86$ (Osterbrock & Ferland 2006). We assume the reddening curve $k(\lambda)$ of Calzetti et al. (2000), so we may write

$$E(\mathrm{B-V}) = 1.97 \log_{10}\left[\frac{(\mathrm{H}\alpha/\mathrm{H}\beta)_{\mathrm{obs}}}{2.86}\right] \quad (1)$$

(i.e. see Domínguez et al. (2013)). We combine this with the relation $A_{\mathrm{V}} = (4.05 \pm 0.80) \times E(B-V)$ from Calzetti et al. (2000) to calculate the extinction $A_{\mathrm{V,HII}}$ from the Hα and Hβ flux measured for each stack.

3.2. *Integrated stellar A_{V}*

We first investigate $A_{\mathrm{V,HII}}$ in bins of $A_{\mathrm{V,star}}$, to better constrain the currently contested relationship between the two for high-redshift galaxies. We choose bins of $A_{\mathrm{V,star}}$ to probe the full range of integrated stellar dust extinction in our sample, from low to medium to high extinction. We define our bins as: $0 \le A_{\mathrm{V}} < 0.6$, $0.6 \le A_{\mathrm{V}} < 1.2$, $1.2 \le A_{\mathrm{V}} < 3.0$. We stack the spectra in these bins and measure $A_{\mathrm{V,HII}}$ on the stack using the relations given in Section 3.1. The results are shown in Figure 3 .

We perform a least-squares ratio fit to the data with a significant ($\geq 2\sigma$) Hβ detection. The best-fit relation is

$$A_{\mathrm{V,HII}} = 1.81^{+0.69}_{-0.43}\, A_{\mathrm{V,star}}, \quad (2)$$

indicating that on average $A_{\mathrm{V,HII}}$ is 1.81 times higher than $A_{\mathrm{V,star}}$ in star forming galaxies at $z \sim 1.5$. This is a slightly lower amount of extra extinction than the ratio of 2.27 which Calzetti et al. (2000) find for low redshift star-forming galaxies, but they are consistent within the errors. Our results are inconsistent with the assumption of no extra dust extinction towards star-forming regions (e.g., as in Erb et al. 2006b, for agreement between Hα and UV SFRs).

Our finding is consistent with that of Wuyts et al. (2013), who find an average relation between $A_{\mathrm{V,star}}$ and $A_{\mathrm{extra}} = (A_{\mathrm{V,HII}})_{\mathrm{HII}} - A_{\mathrm{V,star}}$ for galaxies at $0.7 \le z \le 1.5$. Their relation (shown in Figure 3 by the dotted purple line) is the dust extinction required for agreement between Hα SFRs and UV+IR SFRs, or if there was no IR detection, SED SFRs. Our relation is also consistent with the relation Kashino et al. (2013) find by comparing UV and Hα SFR indicators, but is not consistent with the relation they find using the Balmer decrement.

We also show the results without correcting the Hα flux for [NII] (open grey circles). These points significantly overestimate the amount of $A_{\mathrm{V,HII}}$ relative to $A_{\mathrm{V,star}}$, demonstrating

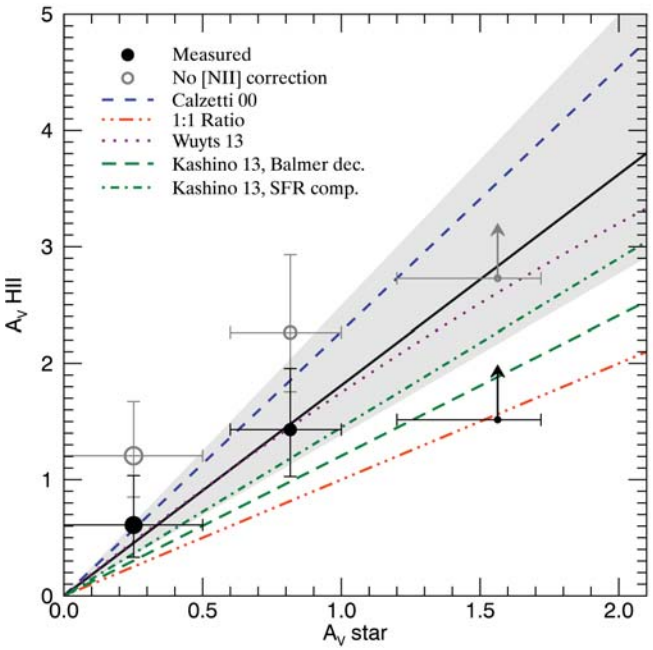

FIG. 3.— $A_{V,\mathrm{star}}$ vs. $A_{V,\mathrm{HII}}$ measured from the spectra stacked in bins of $A_{V,\mathrm{star}}$, shown in the top panel of Fig 2. The black circles show the measured $A_{V,\mathrm{HII}}$ using the Balmer decrement (Hα/Hβ), while the grey open circles show the value of $A_{V,\mathrm{HII}}$ if the blended Hα line was not corrected to remove the [NII] flux. The size of the data points corresponds to the fraction of the total Hα weight in each bin. The $A_{V,\mathrm{star}}$ errors shown are the 1σ scatter within the bins. The blue dashed line shows ratio of $A_{V,\mathrm{HII}}$ to $A_{V,\mathrm{star}}$ from Calzetti et al. (2000). The orange dash-dot-dot line shows the ratio of $A_{V,\mathrm{HII}}$ to $A_{V,\mathrm{star}}$ assuming no extra dust extinction towards emission line regions. The black line shows the best-fit line to our solid data points, which has a slope of 1.81. The fit error is shown with the shaded grey region. This indicates there is extra extinction towards emission line regions, but not as much as Calzetti et al. (2000) finds necessary for low redshift galaxies. Our best-fit line is consistent with the findings of Wuyts et al. (2013), shown with the purple dotted line. The green long dash and green dash-dot lines show the relations found by Kashino et al. (2013).

the necessity of correcting for [NII] when measuring the extinction towards star-forming regions using grism data.

However, it is important to note that there may be significant scatter in the $A_{V,\mathrm{star}}$ and $A_{V,\mathrm{HII}}$ values for individual galaxies, so this result only holds on average for a collection of galaxies.

3.3. *Specific star formation rate*

In this section we probe the change in dust properties over bins of sSFR. We select bins of sSFR to have nearly equal numbers of galaxies per bin, or as close as possible given the SED sSFR values. The bins we use are defined as: $-10.45 \leq \log_{10}\mathrm{sSFR} < -9.31$, $-9.31 \leq \log_{10}\mathrm{sSFR} < -8.92$, $-8.92 \leq \log_{10}\mathrm{sSFR} < -8.10$.

The measured $A_{V,\mathrm{HII}}$ for these stacks are shown in the top left panel of Figure 4. The weighted average $A_{V,\mathrm{star}}$ for the sSFR stacks is also shown. The left panels of Figure 4 show the difference between $A_{V,\mathrm{HII}}$ and $A_{V,\mathrm{star}}$ (ΔA_V, middle) and the ratio $A_{V,\mathrm{HII}}/A_{V,\mathrm{star}}$ (bottom) as a function of sSFR.

There is a small downward trend in $A_{V,\mathrm{star}}$ with increasing sSFR. There is a much more noticeable decrease in $A_{V,\mathrm{HII}}$ with increasing sSFR. We also find a decreasing trend in ΔA_V, which describes the extra extinction towards star-forming regions. (We may write $A_{V,\mathrm{HII}} = A_{V,\mathrm{star}} + A_{V,\mathrm{extra}}$, so $\Delta A_V = A_{V,\mathrm{extra}}$). However, it is unlikely to have negative extra dust extinction towards star-forming regions. The negative value of ΔA_V for the highest sSFR value suggests the $A_{V,\mathrm{star}}$ values for the objects in that bin may be slightly off. To quantify this trend, we perform a least-squares linear fit to $A_{V,\mathrm{extra}}$ vs. log sSFR, and find the best fit relation is

$$A_{V,\mathrm{extra}} = -13.99^{+11.61}_{-4.64} - 1.60^{+1.3}_{-0.52}\ \log_{10}(\mathrm{sSFR}/\mathrm{yr}^{-1}). \quad (3)$$

The ratio $A_{V,\mathrm{HII}}/A_{V,\mathrm{star}}$ is shown for direct comparison with the Calzetti et al. (2000) dust law. On average, the ratio is below the value they find, though it is consistent with their value for the lowest two sSFR bins. The highest sSFR bin is significantly lower than their value. As with ΔA_V, there appears to be a decrease of the ratio with increasing sSFR. This could be explained by the two-phase dust model, as we discuss in Section 4.1.

3.4. *Star formation rate*

Next, we investigate the change in dust properties over bins of SFR. We select bins of SFR to have nearly equal numbers of galaxies per bin. The bins we use are defined as: $-0.26 \leq \log_{10}\mathrm{SFR} < 0.76$, $0.76 \leq \log_{10}\mathrm{SFR} < 1.07$, $1.07 \leq \log_{10}\mathrm{SFR} < 2.02$.

The results for stacks in SFR are shown in the center panel of Figure 4. Both $A_{V,\mathrm{star}}$ and $A_{V,\mathrm{HII}}$ are roughly constant for the lowest and middle SFR bins, and both increase at the highest SFRs.

The trend in ΔA_V shows a low amount of extra extinction for the lowest and middle SFR bins, but it is consistent with zero. The extra extinction for the highest SFR objects is closer to ~ 0.7 on average.

Similar to sSFR, we show the ratio for direct comparison with past work. On average, the ratio is below the value found in Calzetti et al. (2000). There is no apparent trend in the ratio as a function of SFR.

3.5. *Stellar mass*

We also measure dust properties over bins of stellar mass. Bins of stellar mass are chosen to have equal numbers of galaxies per bin. Thus we define the bins as: $8.86 \leq \log_{10}M_* < 9.82$, $9.82 \leq \log_{10}M_* < 10.26$, $10.26 \leq \log_{10}M_* < 11.25$.

The results for the stacks in stellar mass are shown in the right panel of Figure 4. We see an increase in both $A_{V,\mathrm{star}}$ and $A_{V,\mathrm{HII}}$ with increasing stellar mass, with the most massive galaxies being the dustiest.

The plot of ΔA_V shows a roughly constant amount of extra extinction for the smallest and middle mass bins, with $A_{V,\mathrm{extra}} \sim 0.25$. The extra extinction for the highest mass objects is much larger on average, with $A_{V,\mathrm{extra}} \sim 1.5$.

Again, we show the ratio for comparison. On average, the ratio is below the value found in Calzetti et al. (2000), although the smallest and largest mass bin ratios are consistent with their value. There is no apparent trend in the ratio as a function of stellar mass.

4. DISCUSSION

4.1. *Physical interpretation*

The observed extra extinction towards emission line regions, and the decrease in the amount of extra extinction with increasing sSFR are consistent with a two-component dust model (see Calzetti et al. 1994; Charlot & Fall 2000; Granato et al. 2000; Wild et al. 2011). This model assumes there is a diffuse (but possibly clumpy) dust component in the ISM that

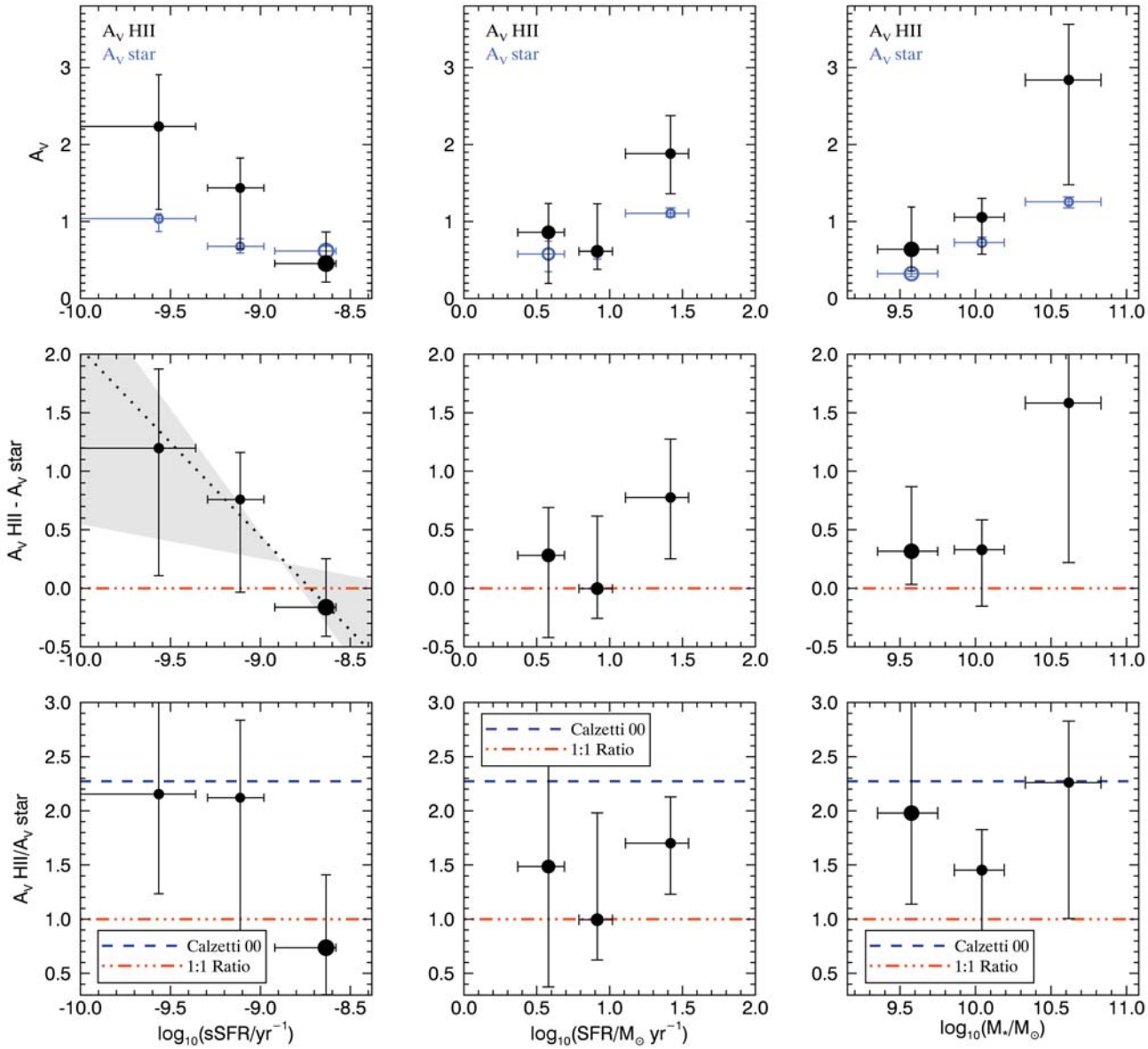

FIG. 4.— A_V measurements for bins in log sSFR, log SFR and $\log M_*$. The top row shows $A_{V,\,\rm star}$ and $A_{V,\,\rm HII}$ vs. the binned parameters. The middle row shows the difference between emission and stellar A_V vs. the binned parameters. The orange dash-dot-dot line shows the case of no extra extinction towards star-forming regions. The bottom row shows the ratio of $A_{V,\,\rm HII}$ to $A_{V,\,\rm star}$ vs. the binned parameters. The blue dashed and orange dash-dot-dot lines in the third row are the ratio between emission A_V and stellar A_V used in Calzetti et al. (2000) and the case of no extra extinction towards star-forming regions, respectively. The size of the data points is described in Fig. 3. The errors in log sSFR, log SFR and $\log M_*$ are the 1σ scatter within the bins. In the center left panel the black dotted line shows the best-fit relation of $A_{V,\,\rm extra} = A_{V,\,\rm HII} - A_{V,\,\rm star}$ vs. log sSFR, with the fit errors shown with the shaded grey region.

affects both the older stellar populations and star-forming regions, as well as an optically thick dust component associated with the short-lived stellar birth clouds that only affects the stars within those regions.

Under the two-phase model, we expect the galaxies with the highest sSFRs to have the continuum light dominated by young, massive stars. These massive stars would predominately still reside in the birth clouds, so both the emission lines and the continuum features would be attenuated by both the birth cloud and the diffuse dust components, resulting in $A_{V,\,\rm HII} \approx A_{V,\,\rm star}$. Galaxies with lower sSFRs would have a smaller continuum contribution from massive stars, so more of the continuum light would come from stars only attenuated by the diffuse dust, resulting in $A_{V,\,\rm HII}$ greater than $A_{V,\,\rm star}$. These different cases are illustrated in Figure 5.

Our result of extra extinction towards star-forming regions is consistent with studies of local starburst galaxies (e.g. Calzetti et al. 2000), with the notable difference that the amount of extra extinction they measure is larger than what we find. In order to understand this difference, we examine the extra dust-corrected equivalent widths of the Balmer lines as a proxy for sSFR, and find the Hα equivalent widths for the galaxies used by Calzetti et al. (2000) (discussed in Calzetti et al. 1994) are much smaller than is measured for our stacks. This may imply that the Calzetti et al. sample has lower sSFRs than our sample, so we would expect a larger amount of extra extinction for their sample than for ours. However, Hα equivalent widths may not be accurate sSFR indicators for very dusty systems. In addition, comparisons between the two samples are not entirely straight-forward, as the Calzetti

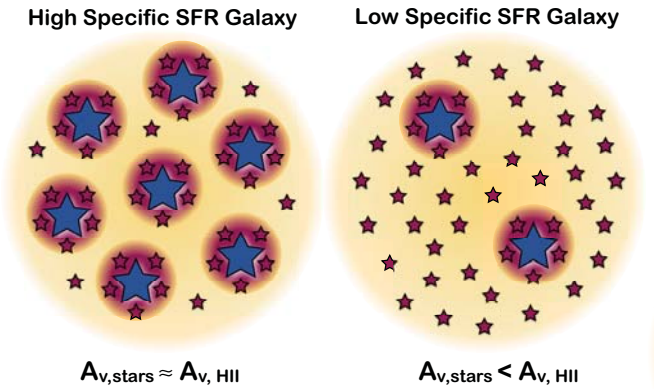

FIG. 5.— Illustration of the two-component dust model in galaxies with high (left panel) and low (right panel) specific SFRs. The yellow regions indicate the diffuse dust component in the ISM. The red regions indicate the optically thick dust component associated with the short-lived stellar birth clouds. The large blue stars show the young, massive stars which mostly are found in the birth clouds. The small red stars show the less massive stars (both young and old), which are found both within the birth clouds and elsewhere. For galaxies with higher specific SFRs, we expect the continuum light to be dominated by the young, massive stars in the birth clouds, so both the continuum and emission lines are attenuated by both dust components. Galaxies with lower specific SFRs would have a higher contribution to the continuum emission from less massive stars, which generally reside outside the birth clouds and are only attenuated by the diffuse dust component, while the emission lines are still attenuated by both dust components. Thus this leads to larger differences between $A_{V,\,star}$ and $A_{V,\,HII}$.

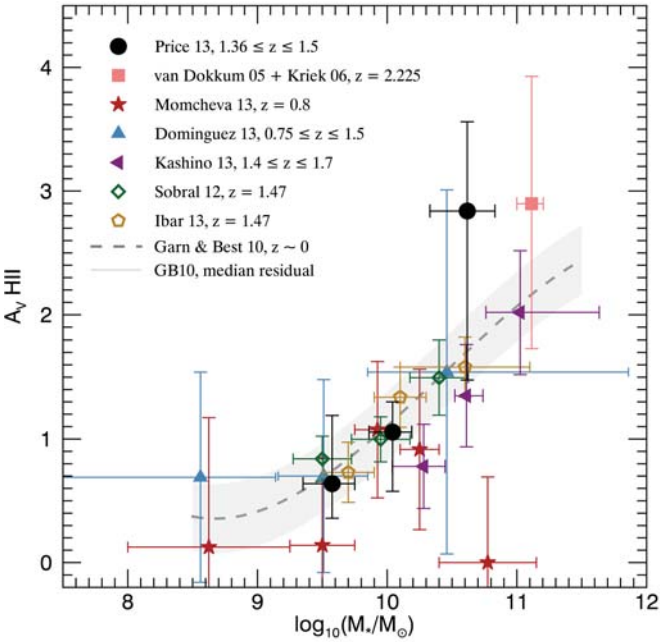

FIG. 6.— $A_{V,\,HII}$ vs. stellar mass comparison between this work and past studies. The filled data (this work; van Dokkum et al. 2005; Momcheva et al. 2013; Domínguez et al. 2013; Kashino et al. 2013) indicate direct measurements of $A_{V,\,HII}$ using Balmer decrements, while the open data indicate $A_{V,\,HII}$ measured with a different method that is calibrated using Balmer decrements. The dashed line gives the median relation derived by Garn & Best (2010) using SDSS star-forming galaxies. With the exception of the single object from van Dokkum et al. (2005) (combined with information from Kriek et al. 2006), all other data are the result of stacks (using various stacking schemes, both mean and median) or are mean (Momcheva et al. 2013, combined with stacking) or median values (Garn & Best 2010; Sobral et al. 2012) of individual objects.

et al. sample lies above the local star-forming main sequence (which may be indicative of mergers) while ours lies along the star-forming main sequence.

A more straight-forward and fair comparison is between our findings and those of Wild et al. (2011), as their sample most likely covers the full local star-forming main sequence. At the highest sSFRs they find similar amounts of extra extinction as Calzetti et al. (2000). They also find increasing amounts of extra extinction with decreasing sSFRs, in agreement with the trend we observe. Wild et al. find higher amounts of extra extinction than we do, but the average sSFRs of their sample are lower than for our sample. The two-phase dust model naturally explains this difference, based on the dependence of extra attenuation on sSFR as discussed above (i.e. lower sSFRs lead to larger amounts of extra extinction) for distant galaxies and observed in local galaxies by Wild et al. (2011).

Along the same lines, the two-component dust model could explain the discrepancies found between different high-redshift studies, if the samples consist of galaxies with different ranges in specific SFR. For example, the Kashino et al. (2013) SFR-M_* relation implies a higher average sSFR than our sample, and they find a lower amount of extra attenuation. Erb et al. (2006a) find evidence for no extra extinction, but the average sSFR is even higher than for the Kashino et al. sample.

Our explanation for the trend between extra A_V and sSFR was previously mentioned by Wild et al. (2011). They suggest that the trend may alternatively be caused by a decline in diffuse dust with decreasing sSFR. However, we observe $A_{V,\,star}$ increases slightly with decreasing sSFR, so we do not expect a decline in diffuse dust with decreasing sSFR.

In absolute terms, we find that $A_{V,\,HII}$ increases with mass and SFR, and decreases with sSFR. As stellar mass and SFR are correlated, the trend of increasing dustiness with SFR and mass could share the same cause. As the trend with increasing mass is stronger, it is likely that mass is the key property. The physical cause may be that more massive objects are able to retain a higher fraction of produced metals, or the cause may be that lower mass galaxies have larger gas fractions, which includes a large amount of less enriched gas.

4.2. *Dust extinction vs. axial ratio*

The two-phase dust model also predicts a dependence of dust attenuation properties on the axial ratio. Under this model, the amount of dust attenuation from the stellar birth clouds is similar in face-on or edge-on systems, while the longer path length in edge-on systems results in a larger overall $A_{V,\,star}$ and a smaller amount of extra attenuation towards the star-forming regions. Wild et al. (2011) find evidence for the two-phase model from the trends of extinction with axial ratio for objects in the local universe.

The spatially resolved WFC3 images yield excellent axial ratio measurements. However, the axial ratio distribution for our sample is heavily biased towards face-on systems. The more edge-on systems may be dustier, so our selection criteria likely introduce this bias against edge-on systems. It might also be that our sample objects are not disk-like galaxies. There may also be a correlation between the completeness fraction and axial ratio. Because of sample incompleteness and the small range in axial ratios, we are unable to test the two-phase model using the inclinations of the galaxies.

4.3. *Comparison of results for $A_{V,\,HII}$ vs. stellar mass*

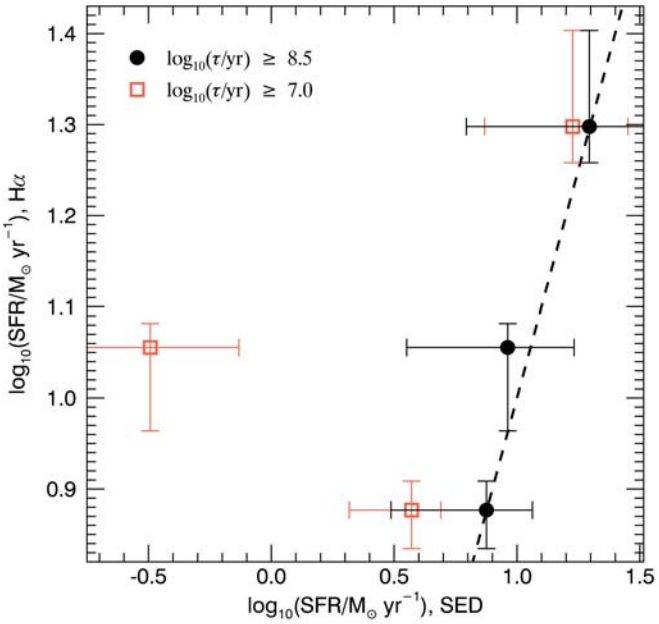

FIG. 7.— Comparison between measured Hα SFRs (Kennicutt 1998) and the SED SFRs. The two sets of SED SFRs differ only in the choice of the minimum star formation e-folding timescale, τ: $\log_{10}(\tau/\mathrm{yr}) \geq 7.0$ (open red squares) and $\log_{10}(\tau/\mathrm{yr}) \geq 8.5$ (closed black circles). (The dashed black line shows equal Hα SFRs and SED SFRs.) The excellent agreement between our Hα SFRs and the SED SFRs calculated with the higher τ_{min} provide an independent verification that setting $\tau_{min} \sim 300$ Myr yields the most reasonable SED fits for star-forming galaxies. (See Section 4.4 for a full discussion.)

A number of past studies have measured Balmer decrements (and often $A_{V,\mathrm{HII}}$) versus stellar mass (Kashino et al. 2013; Domínguez et al. 2013; Momcheva et al. 2013; van Dokkum et al. 2005). Other studies have employed different methods of measuring $A_{V,\mathrm{HII}}$ versus stellar mass. These include comparing L_{IR} to $L_{\mathrm{H}\alpha}$ as by Ibar et al. 2013, or calibrating [OII]/Hα ratio as an alternate to Balmer decrements as by Sobral et al. 2012. We compare our results with their findings in Figure 6.

The collection of results over a range of redshifts makes it tempting to speculate that there is no redshift evolution in the mass-$A_{V,\mathrm{HII}}$ relation. However, the current data are not conclusive. First, there is noticeable scatter in the relation as well as incompleteness at the high mass end. Second, the measurements of $A_{V,\mathrm{HII}}$ are not necessarily equivalent.

The samples of Domínguez et al. (2013) and Kashino et al. (2013) are similar to ours in redshift and method (stacking) for measuring $A_{V,\mathrm{HII}}$. Our data show some disagreement at high masses (although are consistent within the errors), but this may be explained by differences in the galaxy samples or analysis methods. Concerning the work by Domínguez et al. (2013), we first note that their sample contains fewer objects than our sample. Second, we have a broad range of deep photometric coverage for our objects, which reduces the errors in our masses taken from SED modeling. We also do not combine measurements between different grisms, to avoid possible normalization mismatches affecting the line fluxes. Compared with Kashino et al. (2013), our sample is non-targeted and on average has lower sSFRs. The trend we observe between $A_{V,\mathrm{HII}}$ and sSFR shows that the average $A_{V,\mathrm{HII}}$ decreases with increasing sSFR, which explains why their values of $A_{V,\mathrm{HII}}$ are lower than what we measure for similar masses.

4.4. *Implications for Hα SFR compared with SED SFR*

With our direct dust measurements towards HII regions, we can for the first time determine corrected Hα SFRs using the relation by Kennicutt (1998) for a large sample of high redshift galaxies. In this section we use these Hα SFRs (taken from stacks in SFR) to test the much more debated SED SFRs.

The comparison of SFR indicators is shown in Figure 7. We compare Hα SFRs measured from bins in SFR and the corresponding average SED SFRs derived with fitting parameters that include an exponentially decaying SFH and a minimum e-folding time of $\log_{10}(\tau_{\mathrm{min}}/\mathrm{yr}) = 8.5$ (shown as filled black circles). For these SED fitting parameters, we find there is excellent agreement between the Hα and SED SFRs.

This is in agreement with the work of Wuyts et al. (2011b). They compare UV+IR and SED SFRs and find excellent agreement between the SFR indicators for $\log_{10}(\tau_{\mathrm{min}}/\mathrm{yr}) = 8.5$. They also compare the SFR indicators when a shorter exponential decay time of $\log_{10}(\tau_{\mathrm{min}}/\mathrm{yr}) = 7.0$ is adopted, but in that case they find that the SED SFRs underestimate the true SFRs. We repeat our analysis, using the same object groupings for stacking and identical SED fitting parameters with the substitution of $\log_{10}(\tau_{\mathrm{min}}/\mathrm{yr}) = 7.0$ (shown as open red squares). When we allow shorter decay times, we also find the SED SFRs are lower, sometimes significantly, than the Hα SFRs, in agreement with the findings of Wuyts et al. (2011b).

Reddy et al. (2012) also compare UV+IR SFRs with SED SFRs. However, instead of using a longer τ_{min} for a decreasing SFH, they find the SED SFRs agree with UV+IR SFRs when increasing SFHs are adopted. Though increasing SFHs may also give similar results, they are not necessary in order to produce SED SFRs that are in agreement with the Hα SFRs in this work.

4.5. *AGN contamination*

As discussed in Section 2.2, we use a number of methods to reject AGNs from our sample, in order to avoid biasing our probe of dust specifically in star-forming regions. However, as almost all individual objects do not have sufficient line SNRs, and more importantly we do not have separate [NII] and Hα measurements, we cannot use a BPT (Baldwin et al. 1981) diagram to distinguish whether the line emission originates from star formation or AGN.

After stacking, there is sufficient line SNR to place the binned values in the BPT and alternative diagrams, which we show in Figure 8. These diagrams allow us to assess if there is significant AGN contamination in the stacks. We use the data from the stacks in stellar mass in these diagrams.

In the left panel, we show the traditional BPT diagram: [NII]/Hα vs. [OIII]/Hβ. Included are the theoretical limit for star-forming (SF) galaxies from Kewley et al. (2001) (dashed line) and the more conservative empirical division between SF galaxies and AGN by Kauffmann et al. (2003) (dashed-dot line), both of which are derived for galaxies at $z \sim 0$. The SDSS DR7 galaxies (Abazajian et al. 2009) are divided into three categories based on these dividing lines: SF galaxies (blue contours), composite (green contours), and AGN (red contours). These same group definitions are used in the alternate BPT diagrams (middle and right of Figure 8). Because we do not measure [NII] directly (instead inferring a value as described in Section 2.4.1), we cannot use the traditional BPT diagram as a post-analysis check. However, we still can see if our inferred [NII]/Hα ratio is sane given the observed

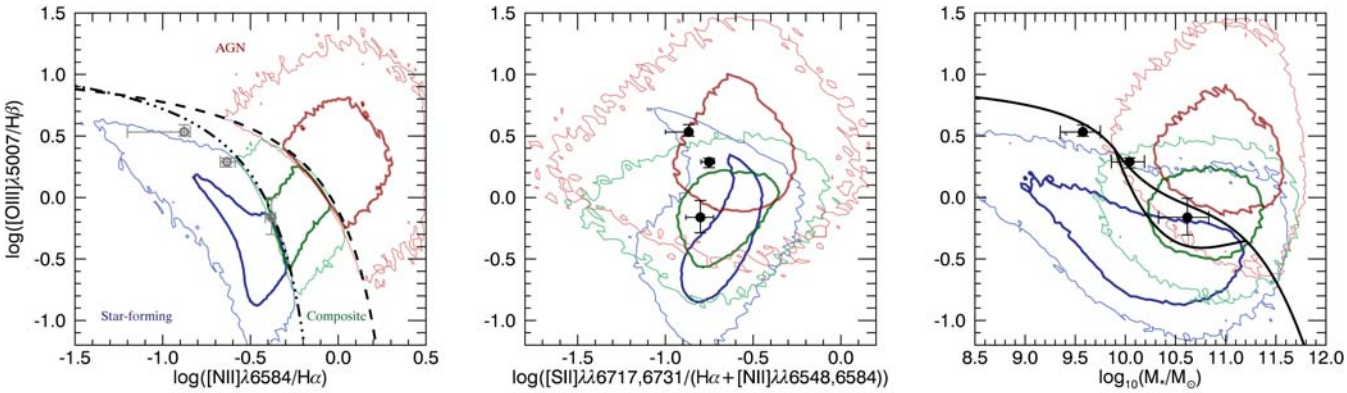

FIG. 8.— Left: Traditional BPT (Baldwin et al. 1981) diagram used to identify the ionizing mechanism for optical emission lines. The dashed line is the theoretical limit between star-forming (SF) galaxies and AGN, as derived in Kewley et al. (2001), and the dashed-dot line is the empirical division derived in Kauffmann et al. (2003) for galaxies in the SDSS. The color contours represent SDSS galaxies, divided into three regions according to these dividing lines. The darker, thicker lines enclose 68% of the population, while the ligher, thinner lines enclose 95%. The grey open points represent our stacked spectra (in bins of M_*), with the [NII]/Hα measurement inferred from the average stellar masses (i.e. not directly measured from the data.) Middle: alternative BPT diagram, using the blended lines observed with the grism. Color contours correspond to the SDSS galaxies in the left panel. The black circles show the measurements from our stacked spectra. This panel illustrates that the combination of blended emission lines does not enable us to discriminate between SF galaxies and AGN. Right: the Mass-Excitation (MEx) diagnostic from Juneau et al. (2011), where the solid lines are the empirical divisions between SF galaxies and AGN, valid for $z < 1$ galaxies. Our stacked spectra (black circles) lie a bit above the division between SF galaxies and AGN, but recent studies have shown that high redshift SF galaxies tend to be offset up and to the right from lower redshift SF galaxies in this diagram (see Section 4.5).

[OIII]/Hβ ratio, which we plot as open grey circles to emphasize that these are not real measurements. We note that the data do lie within the conservative star forming galaxy region, so our inferred [NII]/Hα ratios are consistent with values for SF galaxies. However, in agreement with other observational (e.g. Shapley et al. 2005; Liu et al. 2008) and theoretical studies (Kewley et al. 2013) of distant galaxies, the data points are moved slightly up and right in the BPT diagram compared to the local star-forming sequence.

An alternate BPT diagram, used in Domínguez et al. (2013), is [SII]/Hα vs. [OIII]/Hβ. However, Hα is not a directly measured quantity, so using the deblended Hα values makes it impossible to detangle the assumptions of the [NII] correction with the possible presence of AGN. Instead, we make an alternate diagram with only directly measured quantities: [SII]/(Hα+[NII]) vs. [OIII]/Hβ, which we show in the middle panel of Figure 8. There is significant overlap between the different categories of SDSS galaxies, so we are unable to discriminate between SF galaxies and AGN using combinations of blended emission lines.

A final alternate to the BPT diagram, the Mass-Excitation (MEx) diagram (Juneau et al. 2011), is useful as we directly measure the necessary lines ([OIII] and Hβ) and measure stellar mass with SED fitting, which we show in the right panel of Figure 8. The solid black lines are their empirical divisions between SF, composite, and AGN (valid up to $z \sim 1$). We include the SDSS categories (using stellar masses from the MPA/JHU value-added catalogs; Kauffmann et al. 2003) to demonstrate that while the separation is not as clean as the traditional BPT diagram, it does separate SF galaxies from AGN in the local universe. Our data lie above and to the right of the SF region as defined by Juneau et al. (2011). However, recent work at high-z (Newman et al. 2013) has shown that the low redshift empirical divisions in the MEx diagram incorrectly classify high-z SF galaxies as AGN. They use the shift in the mass-metallicity relation between $z \sim 0$ and 2 to derive a shift left (to lower mass) to bring the high-z values into agreement with the $z \sim 0$ MEx diagram (see Fig. 15 of Newman et al. 2013). With such a shift, our data shifts securely into the SF region of the diagram. This demonstrates that there is likely not much AGN contamination in our data sample.

4.6. *[NII] contamination*

One of the largest sources of uncertainty in this analysis is our correction for [NII] in our measurement of Hα from the blended Hα+[NII] line. Figure 3 demonstrates how much our results change when we do not correct for [NII]. We use the relation between [NII]/Hα and stellar mass by Erb et al. (2006a) as a way of detangling the blended lines. We infer the [NII] contribution from the weighted average mass of each stack. Because the two samples have similar masses and SFRs, and are close in redshift, the average sample properties should be fairly similar. Still, the use of this relation may introduce bias into our results.

If the gas phase metallicities of the Erb et al. (2006a) sample are on average lower than for our sample, for example due to the fact that their sample is at slightly higher redshift ($z \sim 2$), we may be underestimating the [NII] contamination. Also, it is possible there is some AGN contamination at the highest masses (Kriek et al. 2007), which would also result in an underestimate of the [NII] fraction. Finally, the difference in stellar mass definition (Erb et al. use the integrated SFH, while we use the current stellar mass), even after our attempt to correct for the difference in definition, may result in discrepant masses and thus biases in the [NII] correction.

In most cases, our measured Hα flux would be higher than the true value, leading to an overestimate of $A_{\rm V,HII}$. Also, the integrated stellar $A_{\rm V}$ and mass are correlated. Thus if the [NII]/Hα versus mass relation is incorrect, there may be a systematic offset of $A_{\rm V,HII}$ at high mass or $A_{\rm V,star}$.

4.7. *Incompleteness and other systematic uncertainties*

One of the strengths of our analysis is we draw a sample from a non-targeted grism survey, with sample cuts designed to avoid bias as much as possible. However, bias and incompleteness most likely still affect our sample.

The dustiest star-forming galaxies have very attenuated Hα fluxes. Our Hα SNR selection cut, designed to avoid adding noise to our analysis, introduces bias against galaxies with large $A_{\rm V,HII}$. Given the galaxy distribution in Figure 1, the incompleteness of the most dusty galaxies will result in missing the most massive star-forming galaxies, and possibly some of the highest SFR galaxies.

Our continuum normalization scheme also introduces bias into our analysis. We adopt a normalization scheme to improve the signal of our stack, but the cost is that some objects have much higher scaled Hα fluxes, and thus they dominate our stacks. This biases our results towards those objects with higher Hα equivalent widths in a given bin. Because the line measurements are biased based on the Hα flux, we take the weighted average of the continuum values within a bin to ensure a fair comparison. However, if we instead used a non-weighted average, the $A_{\rm V,star}$ vs. $A_{\rm V,HII}$ relationship does not change much.

Finally, the $A_{\rm V,star}$ derived from SED fitting may suffer from severe systematic uncertainties. For example, assuming a fixed attenuation law, implemented as a simple screen leads to biases in the integrated dust attenuation measurements (e.g., Kriek & Conroy 2013). Degeneracies with other modeling parameters may also lead to biases. Including rest-frame mid-IR data in future work will ensure more accurate values of $A_{\rm V,star}$.

5. SUMMARY

In this paper, we investigate dust attenuation in distant star-forming galaxies using data from the 3D-HST survey. We measure both the dust towards HII regions, using Balmer decrements, and the integrated dust properties, using SED modeling. We find that there is extra extinction towards star-forming regions. On average the total attenuation of these regions, $A_{\rm V,HII}$, is 1.81 times the integrated dust attenuation, $A_{\rm V,star}$.

However, the amount of extra attenuation is not the same for all galaxies. We find that the amount of extra attenuation decreases with increasing sSFR, in agreement with the results by Wild et al. (2011) for low-redshift galaxies. The extra extinction also increases with increasing SFR and stellar mass. Our findings are consistent with the two-phase dust model, which assumes there is a diffuse dust component in the ISM and an optically thick dust component associated with the short-lived stellar birth clouds. For galaxies with high sSFR, the stellar light will be dominated by continuum emission from the younger stellar population in the birth clouds, resulting in similar attenuation toward the line and continuum emission. For more evolved galaxies, much of the stellar light will only be attenuated by the diffuse ISM, leading to larger discrepancies between the two dust measures.

Similar to previous studies (Förster Schreiber et al. 2009; Yoshikawa et al. 2010; Wuyts et al. 2011b, 2013; Kashino et al. 2013), we find less extra extinction in distant galaxies than is found in the local universe (Calzetti et al. 2000). This effect can also be explained by the two-phase model, as lower redshift objects tend to have lower sSFRs than higher redshift galaxies (e.g. Noeske et al. 2007; Whitaker et al. 2012b; Fumagalli et al. 2012).

We also find that both $A_{\rm V,HII}$ and $A_{\rm V,star}$ increase with increasing SFR and stellar mass, and decreasing specific SFRs. This illustrates that more massive galaxies with higher SFRs are also more dusty in general. This is generally consistent with previous studies of $A_{\rm V,HII}$ and stellar mass over a wide range of redshifts. We also observe there to be little redshift evolution in the $A_{\rm V,HII}$-M_* relation, although errors and incompleteness makes it impossible to make a definite claim.

We use our corrected Hα SFRs to test the accuracy of SFRs derived from SED fitting. We find excellent agreement between the SFR indicators if short SFH decay times are not allowed and the constraint $\log_{10}(\tau/{\rm yr}) > 8.5$ is used. This independently confirms the results of past studies comparing UV+IR and SED SFRs (Wuyts et al. 2011b) or Hα and SED SFRs (Wuyts et al. 2013).

We note that our results are slightly impacted by incompleteness and systematic uncertainties. First, we employ SNR cuts on Hα to ensure quality data, but this likely results in incompleteness of the dustiest galaxies. Second, to obtain significant Hβ detections, we stack spectra, and thus our normalization scheme or incorrectly measured integrated properties could impact our measurements. Finally, grism spectra have low spectral resolution, so we deblend the Hα and [NII] emission lines using a metallicity-derived [NII] correction scheme, which could introduce systematic bias to our results as well.

Most of these issues can be overcome with future observations by a number of new multi-object near infrared spectrographs on 8-10 m class telescopes, among which is MOSFIRE on Keck (McLean et al. 2010). These instruments have higher spectral resolutions, which will avoid blended lines. They will also allow for deeper measurements, which will yield more accurate Balmer decrements of individual objects as well as allowing for investigation of dust to higher $A_{\rm V}$ limits.

We thank Edward Taylor for useful discussions, and David Sobral for sharing results for comparison. This work is based on observations taken by the 3D-HST Treasury Program (GO 12177 and 12328) with the NASA/ESA HST, which is operated by the Association of Universities for Research in Astronomy, Inc., under NASA contract NAS5-26555. We acknowledge support from STScI grant 12117.17-A. SP is funded by the National Science Foundation Graduate Research Fellowship under Grant No. DGE 1106400.

REFERENCES

Abazajian, K. N., Adelman-McCarthy, J. K., Agüeros, M. a., et al. 2009, ApJS, 182, 543
Alexander, D. M., Bauer, F. E., Brandt, W. N., et al. 2003, AJ, 126, 539
Atek, H., Malkan, M., McCarthy, P., et al. 2010, ApJ, 723, 104
Baldwin, J. A., Phillips, M. M., & Terlevich, R. 1981, PASP, 93, 5
Bauer, F. E., Alexander, D. M., Brandt, W. N., et al. 2002, AJ, 124, 2351
Bouwens, R. J., Illingworth, G. D., Oesch, P., et al. 2012, ApJ, 754, 83
Brammer, G. B., van Dokkum, P. G., & Coppi, P. 2008, ApJ, 686, 1503
Brammer, G. B., van Dokkum, P. G., Franx, M., et al. 2012, ApJS, 200, 13
Brinchmann, J., Charlot, S., White, S. D. M., et al. 2004, MNRAS, 351, 1151
Bruzual, G., & Charlot, S. 2003, MNRAS, 344, 1000
Calzetti, D., Armus, L., Bohlin, R. C., et al. 2000, ApJ, 533, 682
Calzetti, D., Kinney, A. L., & Storchi-Bergmann, T. 1994, ApJ, 429, 582
Chabrier, G. 2003, PASP, 115, 763
Charlot, S., & Fall, S. M. 2000, ApJ, 539, 718
Conroy, C. 2013, ARA&A, 51, 393
Conroy, C., Schiminovich, D., & Blanton, M. R. 2010, ApJ, 718, 184
Daddi, E., Dickinson, M., Morrison, G., et al. 2007, ApJ, 670, 156
Domínguez, A., Siana, B., Henry, A. L., et al. 2013, ApJ, 763, 145
Donley, J. L., Koekemoer, A. M., Brusa, M., et al. 2012, ApJ, 748, 142
Draine, B. T., Dale, D. a., Bendo, G., et al. 2007, ApJ, 663, 866
Erb, D. K., Shapley, A. E., Pettini, M., et al. 2006a, ApJ, 644, 813
Erb, D. K., Steidel, C. C., Shapley, A. E., et al. 2006b, ApJ, 647, 128

Finkelstein, S. L., Papovich, C., Salmon, B., et al. 2012, ApJ, 756, 164
Förster Schreiber, N. M., Genzel, R., Bouché, N., et al. 2009, ApJ, 706, 1364
Fumagalli, M., Patel, S. G., Franx, M., et al. 2012, ApJ, 757, L22
Garn, T., & Best, P. N. 2010, MNRAS, 409, 421
Gonzalez-Perez, V., Lacey, C. G., Baugh, C. M., Frenk, C. S., & Wilkins, S. M. 2013, MNRAS, 429, 1609
Granato, G. L., Lacey, C. G., Silva, L., et al. 2000, ApJ, 542, 710
Hainline, K. N., Shapley, A. E., Kornei, K. a., et al. 2009, ApJ, 701, 52
Hathi, N. P., Cohen, S. H., Ryan, R. E., et al. 2013, ApJ, 765, 88
Ibar, E., Sobral, D., Best, P. N., et al. 2013, arXiv:1307.3556v1
Johnson, B. D., Schiminovich, D., Seibert, M., et al. 2007, ApJS, 173, 392
Juneau, S., Dickinson, M., Alexander, D. M., & Salim, S. 2011, ApJ, 736, 104
Kajisawa, M., Ichikawa, T., Tanaka, I., et al. 2011, PASJ, 63, 379
Kashino, D., Silverman, J. D., Rodighiero, G., et al. 2013, ApJL, accepted, (arXiv:1309.4774)
Kauffmann, G., Heckman, T. M., Tremonti, C., et al. 2003, MNRAS, 346, 1055
Kennicutt, R. C. 1998, ApJ, 498, 541
Kewley, L. J., Dopita, M. A., Leitherer, C., et al. 2013, ApJ, accepted, (arXiv:1307.0508)
Kewley, L. J., Dopita, M. A., Sutherland, R. S., Heisler, C. A., & Trevena, J. 2001, ApJ, 556, 121
Koekemoer, A. M., Faber, S. M., Ferguson, H. C., et al. 2011, ApJS, 197, 36
Kong, X., Charlot, S., Brinchmann, J., & Fall, S. M. 2004, MNRAS, 349, 769
Kriek, M., & Conroy, C. 2013, ApJL, accepted, (arXiv:1308.1099v1)
Kriek, M., van Dokkum, P. G., Labbé, I., et al. 2009, ApJ, 700, 221
Kriek, M., van Dokkum, P. G., Franx, M., et al. 2006, ApJ, 645, 44
—. 2007, ApJ, 669, 776
Liu, X., Shapley, A. E., Coil, A. L., Brinchmann, J., & Ma, C. 2008, ApJ, 678, 758
Ly, C., Malkan, M. A., Kashikawa, N., et al. 2012, ApJ, 747, L16
Mancini, C., Förster Schreiber, N. M., Renzini, A., et al. 2011, ApJ, 743, 86
McLean, I. S., Steidel, C. C., Epps, H., et al. 2010, in Proceedings of SPIE, ed. I. S. McLean, S. K. Ramsay, & H. Takami, Vol. 7735, 77351E–77351E–12
Mendez, A. J., Coil, A. L., Aird, J., et al. 2013, ApJ, 770, 40
Meurer, G. R., Heckman, T. M., & Calzetti, D. 1999, ApJ, 521, 64
Momcheva, I. G., Lee, J. C., Ly, C., et al. 2013, AJ, 145, 47
Nelson, E. J., van Dokkum, P. G., Momcheva, I., et al. 2013, ApJ, 763, L16
Newman, S. F., Buschkamp, P., Genzel, R., et al. 2013, ApJ, submitted, (arXiv:1306.6676)
Noeske, K. G., Weiner, B. J., Faber, S. M., et al. 2007, ApJ, 660, L43
Osterbrock, D. E., & Ferland, G. J. 2006, Astrophysics of gaseous nebulae and active galactic nuclei, 2nd edn. (Sausalito, CA: University Science Books)
Reddy, N. A., Erb, D. K., Pettini, M., Steidel, C. C., & Shapley, A. E. 2010, ApJ, 712, 1070
Reddy, N. A., Pettini, M., Steidel, C. C., et al. 2012, ApJ, 754, 25
Reddy, N. A., Steidel, C. C., Fadda, D., et al. 2006, ApJ, 644, 792
Rosario, D. J., Mozena, M., Wuyts, S., et al. 2013, ApJ, 763, 59
Savaglio, S., Glazebrook, K., Le Borgne, D., et al. 2005, ApJ, 635, 260
Shapley, A. E. 2011, ARA&A, 49, 525
Shapley, A. E., Coil, A. L., Ma, C., & Bundy, K. 2005, ApJ, 635, 1006
Sobral, D., Best, P. N., Matsuda, Y., et al. 2012, MNRAS, 420, 1926
Teplitz, H. I., McLean, I. S., Becklin, E. E., et al. 2000, ApJ, 533, L65
van Dokkum, P. G., Kriek, M., Rodgers, B., Franx, M., & Puxley, P. 2005, ApJ, 622, L13
van Dokkum, P. G., Brammer, G., Fumagalli, M., et al. 2011, ApJ, 743, L15
Villar, V., Gallego, J., PérezâĂŘGonzález, P. G., et al. 2008, ApJ, 677, 169
Watson, M. G., Schröder, A. C., Fyfe, D., et al. 2009, A&A, 493, 339
Whitaker, K. E., Kriek, M., van Dokkum, P. G., et al. 2012a, ApJ, 745, 179
Whitaker, K. E., van Dokkum, P. G., Brammer, G., & Franx, M. 2012b, ApJ, 754, L29
Whitaker, K. E., Labbé, I., van Dokkum, P. G., et al. 2011, ApJ, 735, 86
Wild, V., Charlot, S., Brinchmann, J., et al. 2011, MNRAS, 417, 1760
Wilkins, S. M., Bunker, A. J., Stanway, E., Lorenzoni, S., & Caruana, J. 2011, MNRAS, 417, 717
Williams, R. J., Quadri, R. F., Franx, M., van Dokkum, P., & Labbé, I. 2009, ApJ, 691, 1879
Wuyts, S., Labbé, I., Schreiber, N. M. F., et al. 2008, ApJ, 682, 985
Wuyts, S., Förster Schreiber, N. M., van der Wel, A., et al. 2011a, ApJ, 742, 96
Wuyts, S., Förster Schreiber, N. M., Lutz, D., et al. 2011b, ApJ, 738, 106
Wuyts, S., Förster Schreiber, N. M., Genzel, R., et al. 2012, ApJ, 753
Wuyts, S., Forster Schreiber, N. M., Nelson, E. J., et al. 2013, ApJ, submitted
Xue, Y. Q., Luo, B., Brandt, W. N., et al. 2011, ApJS, 195, 10
Yoshikawa, T., Akiyama, M., Kajisawa, M., et al. 2010, ApJ, 718, 112